

# Magnetron Sputtered SnO<sub>2</sub> Layer Combined with NiCo–LDH Nanosheets for High-Performance All-Solid-State Supercapacitors

Yi Jiang,<sup>\*[a]</sup> Hexiang Hu,<sup>[b]</sup> Ruixiang Xu,<sup>[b]</sup> Hao Gu,<sup>[b]</sup> Limei Zhang,<sup>[a]</sup> Zhengyang Ji,<sup>[a]</sup> Jingwei Zhou,<sup>[a]</sup> Ying Liu,<sup>[a]</sup> and Bin Cai<sup>\*[b]</sup>

Nickel-cobalt layered double hydroxide (NiCo–LDH) has attracted much attention because of its excellent electrochemical properties and regulability. And it is a potential pseudocapacitive electrode material, which is commonly used in supercapacitors and lithium-ion batteries. Its application in the field of supercapacitors can improve the energy density, power density and cycle life of devices. However, NiCo–LDH still faces some challenges, such as poor electrical conductivity and the capacity attenuation caused by agglomeration of layered structures, which require further research and optimization. In this paper, SnO<sub>2</sub> films were prepared on carbon cloth (CC) by

magnetron sputtering method, and Ni–Co LDH nanosheets were grown by hydrothermal reaction to obtain NiCo–LDH@SnO<sub>2</sub> composites. Due to the synergistic effect between NiCo–LDH and SnO<sub>2</sub>, NiCo–LDH@SnO<sub>2</sub> composites exhibit high Cs and good cyclic stability. In addition, an all-solid-state flexible asymmetric supercapacitor (ASC) was assembled with activated carbon (AC) anodes, showing good specific capacitance(Cs) and energy density. And a high initial capacitance can still be retained after 10,000 cycles. This paper shows that NiCo–LDH@SnO<sub>2</sub> shows excellent application potential in supercapacitors.

## 1. Introduction

The shortage of fossil fuels has led to greater need for clean energy sources, but their intermittent nature highlights the importance of energy storage devices.<sup>[1–3]</sup> Thus, greater challenges are presented for the storage devices of clean eneitors stand out among many energy storage devices because of their advantages such as high power density, long cycle life, fast charge-discharge capabiliry sources.<sup>[4–6]</sup> Supercapacity, wide operating temperature range and environmental friendliness.<sup>[7–9]</sup> And they have good prospects in wearable flexible devices, electronics and hybrid vehicles.<sup>[10–13]</sup> The electrode material is a key component of the supercapacitor, which often determines the performance of a capacitor.<sup>[14–16]</sup> The ideal electrode material needs to have the following characteristics, such as large Cs, high conductivity, large specific surface area, good cycle stability, and good safety.<sup>[17–18]</sup>

In recent years, nickel-cobalt layered double hydroxide (NiCo–LDH) have become the research focus of supercapacitor

electrode materials because of their advantages such as ultra-high theoretical capacity, large specific surface area, adjustable layer spacing, long cycle life, and abundant natural reserves, while helping to improve the power density of supercapacitors.<sup>[19–23]</sup> However, NiCo–LDH electrode materials have poor electrical conductivity. Moreover, their lamellar structures are unstable, and there is lamellar agglomeration during the long-term cycle. Despite the limitations of NiCo–LDH, the high specific capacity of NiCo–LDH makes it an important potential for application in supercapacitors. It is an effective scheme to improve the electrochemical performance by combining electrode materials with good electrical conductivity. Zhu et al. combined carbon nanotubes with NiCo–LDH, which not only provided good support for NiCo–LDHs nanosheets, but also improved the mass transfer of ions on the surface of NiCo–LDH.<sup>[24]</sup> Liu et al. prepared Co<sub>9</sub>S<sub>8</sub>@NiCo–LDH core-shell nanotube arrays, which increased the charge transfer rate during redox process and improved their electrochemical energy storage performance.<sup>[25]</sup> Zou et al. used graphene compounded with NiCo–LDH nanosheets to improve the inherent conductivity of NiCo–LDH, resulting in a significant increase in rate capability.<sup>[26]</sup> The above results show that the structural stability and conductivity of NiCo–LDH are effectively improved by the combination with highly conductive electrode materials, and the comprehensive performance of the materials is improved. As the supercapacitor electrode material, SnO<sub>2</sub> has the advantages of high conductivity, good cycle stability, high Cs and low price, and is one of the most concerned materials in the field of supercapacitors.<sup>[27–32]</sup> Through the combination of NiCo–LDH and SnO<sub>2</sub>, the comprehensive properties of the material can be improved, not only the conductivity is improved, but also the pseudocapacitance is

[a] Y. Jiang, L. Zhang, Z. Ji, J. Zhou, Y. Liu

School of Science,  
Changchun Institute of Technology,  
Changchun, 130012, China  
E-mail: jiangyi@ccit.edu.cn

[b] H. Hu, R. Xu, H. Gu, B. Cai

Key Laboratory of Advanced Structural Materials,  
Ministry of Education & Advanced Institute of Materials Science,  
Changchun University of Technology,  
Changchun 130012, China  
E-mail: caibin970210@hotmail.com

 Supporting information for this article is available on the WWW under  
<https://doi.org/10.1002/batt.202400122>

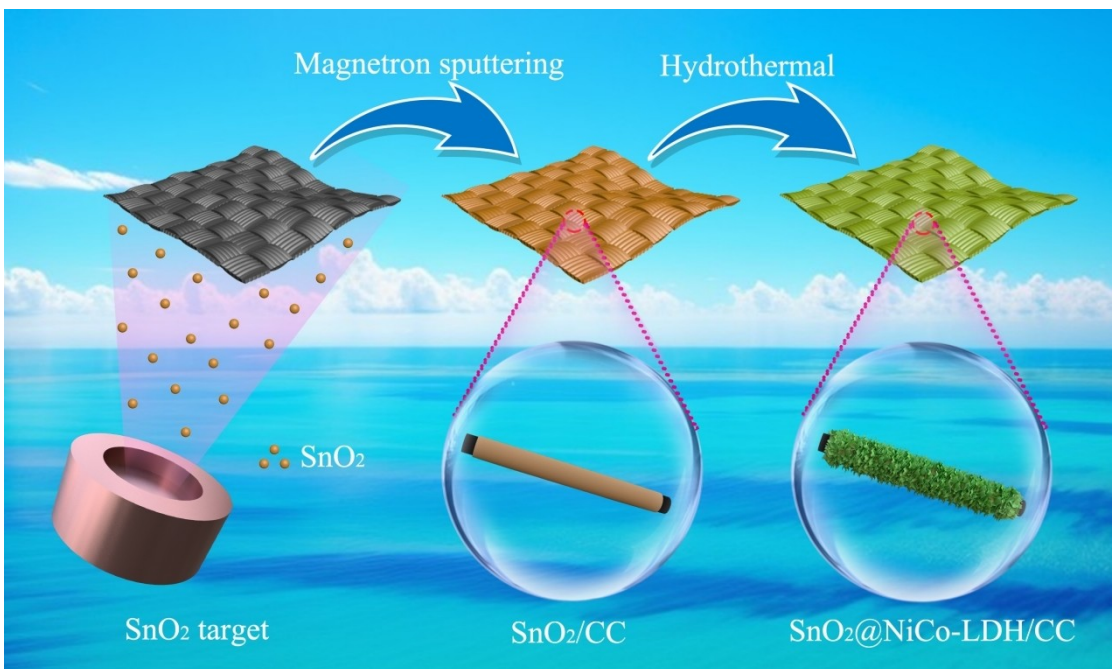


Figure 1. Schematic illustration of synthesis process of NiCo–LDH@SnO<sub>2</sub> composites.

increased. At the same time, the lamellar structure of NiCo–LDH provides quite a few active sites for Faraday redox reaction, so that the composite can store more charges. Therefore, the combination of NiCo–LDH material and SnO<sub>2</sub> material is expected to obtain better electrochemical properties.

In this paper, we used magnetron sputtering technology to prepare SnO<sub>2</sub> film on CC surface. The film prepared by magnetron sputtering has the advantages of high uniformity, dense film layer, high quality, fast deposition rate, and pollution-free production process.<sup>[33–38]</sup> Then NiCo–LDH nanosheets were grown on SnO<sub>2</sub> film by hydrothermal reaction to form NiCo–LDH@SnO<sub>2</sub>. It has an open nanosheet structure, promotes the infiltration of the electrolyte, provides plenty of active sites for the Faraday redox reaction, and exhibits a Cs of 1766 mF cm<sup>-2</sup>. In addition, we have assembled an all-solid-state ASC with a Cs of 710 mF cm<sup>-2</sup> and good cycle stability using the AC negative electrode. Therefore, NiCo–LDH@SnO<sub>2</sub> shows eximious application potential as supercapacitor electrode materials.

## Experimental

### Preparation of Ni–Co LDH@ SnO<sub>2</sub> Composite

Acetone, anhydrous ethanol, and deionized water were used to clean the acidified CC to remove oil and impurities from its surface. And it is dried at 60 °C for 5 h to prepare for the next step of manufacturing supercapacitor electrodes.

First, reactive magnetron sputtering technology was used to prepare bindless SnO<sub>2</sub> film for supercapacitors on the CC surface after acidification. Prior to the sputtering process, the carbon cloth substrates were continuously ultrasonically cleaned in water and

ethanol, respectively, for 15 min. The deposition power was used at 40 W for 30 min. The total deposition pressure was kept constant (3.0 Pa). Then, 2 mmol of cobalt nitrate hexahydrate, 2 mmol of nickel nitrate hexahydrate, 2 mmol of CTAB and 4 mmol of urea were dissolved in 40 ml of methanol, and magnetic stirring was carried out for 30 min to make the mixed solution uniform. Finally, the CC with SnO<sub>2</sub> film and the mixed solution were put into a reactor at 120 °C for 10 h. After the hydrothermal reaction was completed, the surface of the CC was cleaned with a large amount of deionized water, and then dried in a constant temperature drying oven at 60 °C overnight, thus NiCo–LDH@SnO<sub>2</sub> composite material was obtained.

### Assembly of All-Solid-State Flexible ASCs

The black slurry is acquired by hand grinding with AC, acetylene black and PVDF at a mass ratio of 8:1:1. It is then uniformly coated on the CC surface to prepare the AC negative electrode. PVA/KOH gel was prepared using 3 g PVA, 30 ml DIW and 3 M potassium hydroxide. Finally, an all-solid-state ASC is assembled with NiCo–LDH@SnO<sub>2</sub> cathode, AC anode and PVA/KOH gel.

## 2. Results and Discussion

Figure 1 shows the synthesis process of NiCo–LDH@SnO<sub>2</sub> electrode material. Firstly, a homogeneous and dense SnO<sub>2</sub> film was prepared on CC surface by magnetron sputtering technology. Then NiCo–LDH nanosheets were grown on SnO<sub>2</sub> film surface by hydrothermal reaction, and NiCo–LDH@SnO<sub>2</sub> electrode materials were prepared. NiCo–LDH nanosheets successfully improved the electrochemical properties of electrode materials by combining with highly conductive SnO<sub>2</sub>.

Figure 2a displays the X-ray diffraction (XRD) pattern of the NiCo–LDH@SnO<sub>2</sub> composite. The 26.42° diffraction peak comes

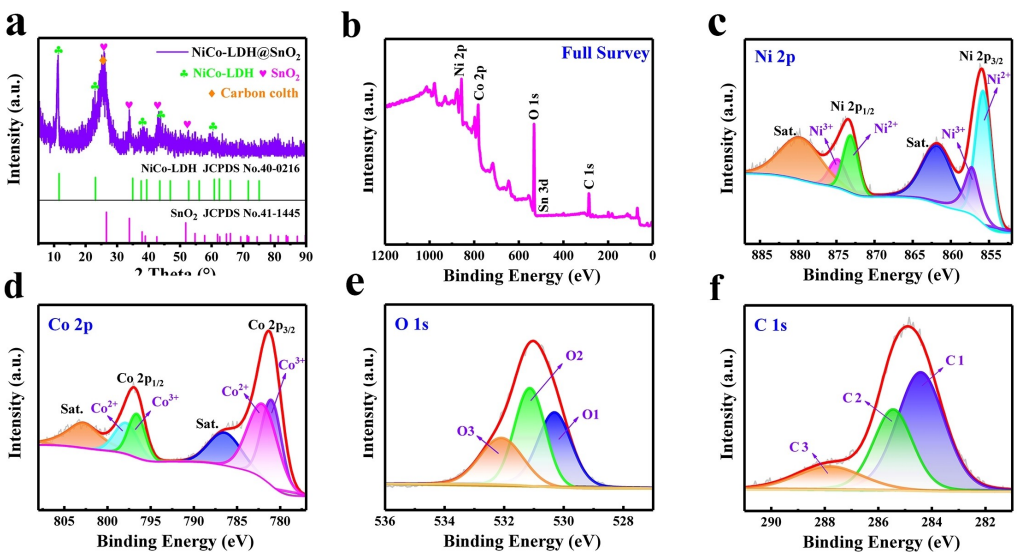


Figure 2. (a) XRD pattern and (b) XPS survey spectrum of NiCo–LDH@SnO<sub>2</sub>; High-resolution spectra of (c) Ni 2p, (d) Co 2p, (e) O 1s and (f) C 1s.

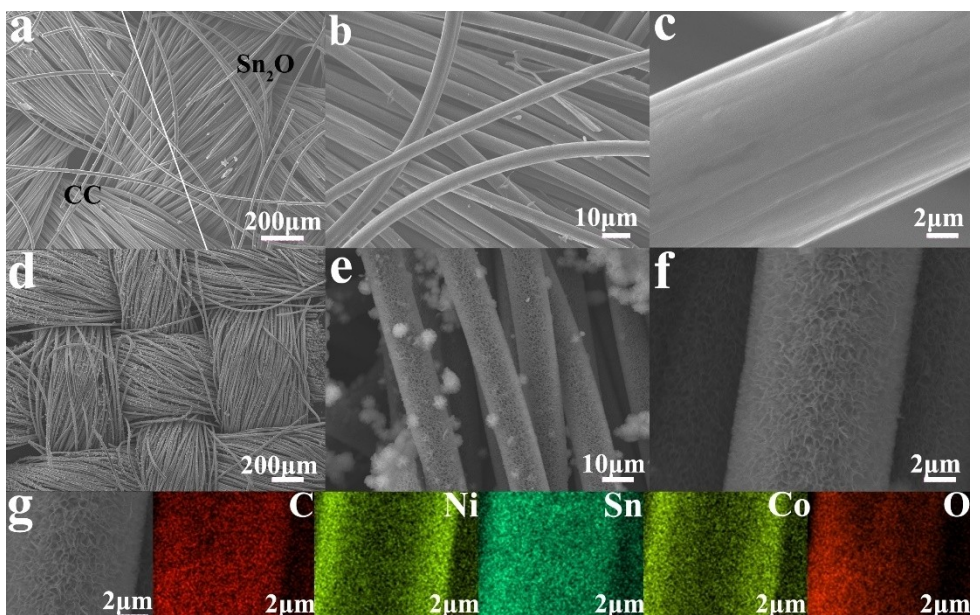


Figure 3. SEM images of both (a-c) SnO<sub>2</sub>@CC ; SEM images of both (d-f) NiCo–LDH@SnO<sub>2</sub>; (g) EDS images of element mapping of C, Ni, Sn, Co, O.

from CC, corresponding to the (006) crystal face of carbon (JCPDS NO.26-1076).<sup>[39]</sup> The diffraction peaks at 26.27, 33.86, 42.84, 52.14° correspond to the (110), (101), (210), and (211) crystal faces of SnO<sub>2</sub> (JCPDS NO.41-1445), respectively.<sup>[40]</sup> The diffraction peaks at 11.28, 22.98, 38.74, 43.82, and 60.52° correspond to (003), (006), (105), (107), and (110) crystal planes of NiCo–LDH (JCPDS NO.40-0216), respectively.<sup>[21]</sup> The successful synthesis of NiCo–LDH@SnO<sub>2</sub> composite was proved by XRD pattern.

In order to further analyze the chemical valence states of the composites, X-ray photoelectron spectroscopy (XPS) analysis was carried out. Figure 2b shows the full XPS spectrum of the sample, where the presence of Ni 2p, Co 2p, O 1s, Sn 3d, and C 1s peaks can be seen. Figure 2c shows the Ni 2p high-

resolution spectrum, demonstrating the presence of Ni 2p<sub>1/2</sub> and Ni 2p<sub>3/2</sub>, which can be decomposed and fitted into two spin orbital bipeaks. The peaks at 873.1 and 855.7 eV correspond to Ni<sup>2+</sup>, and the peaks at 874.8 and 857.2 eV correspond to Ni<sup>3+</sup>. The two peaks at 879.5 and 861.6 eV are satellite peaks of Ni 2p<sub>1/2</sub> and Ni 2p<sub>3/2</sub> states.<sup>[41]</sup>

Figure 2d displays the Co 2p spectrum, where Co 2p<sub>1/2</sub> and Co 2p<sub>3/2</sub> can be decomposed into two spin orbital bipeaks. This indicates the co-presence of Co<sup>2+</sup> (797.8 and 782 eV) and Co<sup>3+</sup> (796.6 and 780.1 eV). And the peaks at 802.7 eV and 785.5 eV correspond to the satellite peaks of Co 2p<sub>1/2</sub> and Co 2p<sub>3/2</sub>.<sup>[42]</sup> Figure 2e displays the O 1s spectrum, which can be decomposed into three peaks: O1 (530.3 eV), O2 (531.2 eV) and O3 (532.1 eV). They revealed the presence of lattice oxygen, oxygen

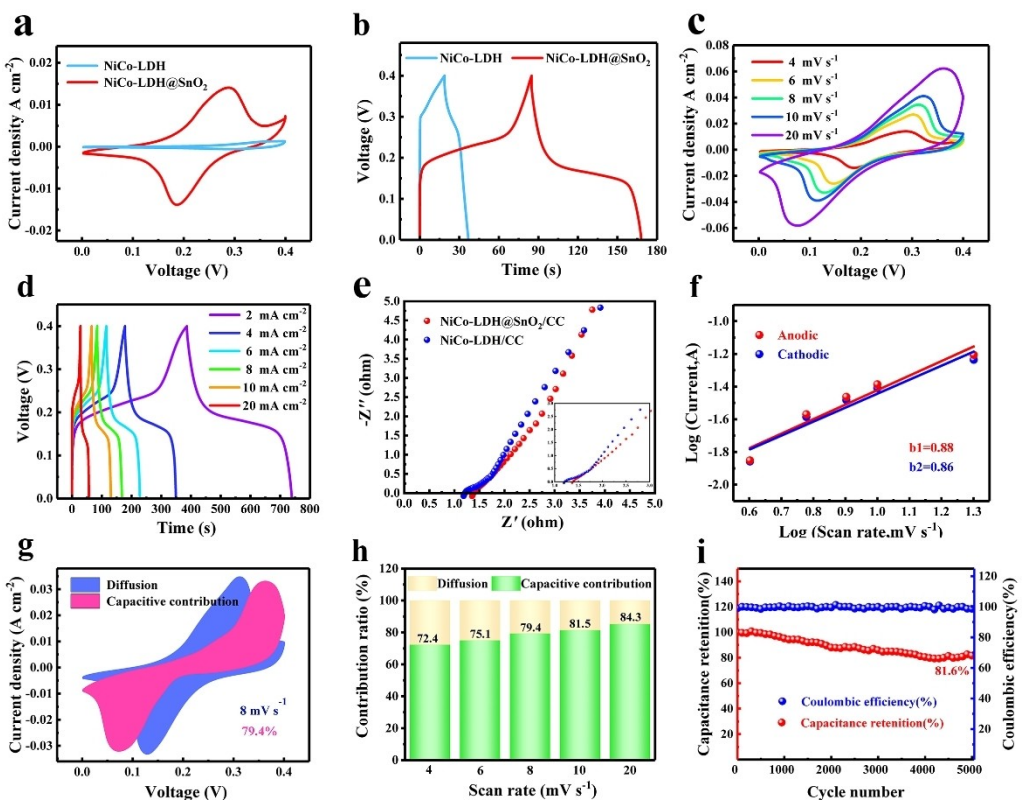


**Figure 4.** (a) CV curves ( $4 \text{ mV s}^{-1}$ ) and (b) GCD curves ( $8 \text{ mA cm}^{-2}$ ) of NiCo–LDH and NiCo–LDH@ $\text{SnO}_2$ ; (c) CV curves and (d) GCD curves of NiCo–LDH@ $\text{SnO}_2$  at different scan rates and current densities, respectively; (e) EIS curves of NiCo–LDH and NiCo–LDH@ $\text{SnO}_2$ ; (f) The plots of  $\log(i)$  vs  $\log(v)$  of NiCo–LDH@ $\text{SnO}_2$ ; (g) Capacitive contribution of NiCo–LDH@ $\text{SnO}_2$  at  $8 \text{ mV s}^{-1}$ ; (h) Ratio of capacitive controlled and diffusion-controlled contribution at different scan rates; (i) Cycleability and Coulombic efficiency of NiCo–LDH@ $\text{SnO}_2$  on CC at  $20 \text{ mA cm}^{-2}$ .

vacancy, and water.<sup>[24]</sup> The  $\text{SnO}_2$  layer prepared by magnetron sputtering is covered by NiCo–LDH nanosheets at the bottom layer, so the detection effect of Sn 3d is not obvious. Figure 2f displays the C1s spectrum, which can be further decomposed and fitted to three peaks C1 (284.4 eV), C2 (285.4 eV) and C3 (287.8 eV), corresponding to the C=C, C–O and O=C–O groups, respectively.<sup>[43]</sup>

Figure 3a–c shows the SEM image of  $\text{SnO}_2$ @CC composite prepared on CC surface. Figure 3d–f shows the SEM images of NiCo–LDH@ $\text{SnO}_2$  composites at different magnifications. It can be seen that the NiCo–LDH nanosheets are compactly coated on the CC surface with  $\text{SnO}_2$ , and the NiCo–LDH nanosheets are interlaced. This unique nanosheet structure promotes the penetration of the electrolyte and facilitates the transport of ions. At the same time, more active sites are provided for Faraday redox reaction, so that NiCo–LDH@ $\text{SnO}_2$  composites are expected to obtain excellent electrochemical properties. In addition, from the element mapping image in Figure 3d, Ni, Co, C, Sn and O elements are evenly dispersed on the surface of the sample, which proves the successful synthesis of NiCo–LDH@ $\text{SnO}_2$  composite materials.

To investigate the electrochemical properties of NiCo–LDH@ $\text{SnO}_2$  composites, cyclic voltammetry (CV), constant current charge-discharge (GCD) and electrochemical impedance spectroscopy (EIS) were used in a three-electrode system containing 3 M KOH electrolyte. Figure 4a shows the CV curves

of NiCo–LDH@ $\text{SnO}_2$  and NiCo–LDH electrode materials at  $4 \text{ mV s}^{-1}$ . It can be seen that the capacity of the composite materials has been significantly improved by the combination with  $\text{SnO}_2$ . Figure 4b presents the GCD curves of NiCo–LDH@ $\text{SnO}_2$  and NiCo–LDH electrode materials at  $8 \text{ mA cm}^{-2}$ . Similarly, NiCo–LDH@ $\text{SnO}_2$  composites exhibit superior electrochemical properties, which have a longer discharge time and means a higher Cs. The reason why NiCo–LDH@ $\text{SnO}_2$  composites exhibit better electrochemical performance is that the heterojunction is formed by the combination of NiCo–LDH and  $\text{SnO}_2$ . The advantages of these two materials are combined to form a new type of material with more excellent properties. In addition, compared with other preparation methods, the  $\text{SnO}_2$  film prepared by magnetron sputtering method is more uniform and dense, and has fewer interface defects, thus reducing the impact of interface defects on the electrode material performance, and is more excellent in terms of electron transport performance. Figure 4c shows the CV curve of NiCo–LDH@ $\text{SnO}_2$  electrode material, which shows the characteristics of battery-type electrode material. The obvious Faraday redox peak indicates that NiCo–LDH@ $\text{SnO}_2$  is a kind of pseudocapacitor material. In the meantime, with the increase of scanning rate, the shape of CV curve remains good, indicating that the Faraday redox reaction occurring at the electrode surface is well reversible. The GCD curves of NiCo–LDH@ $\text{SnO}_2$  in Figure 4d all have an obvious voltage platform, which corre-

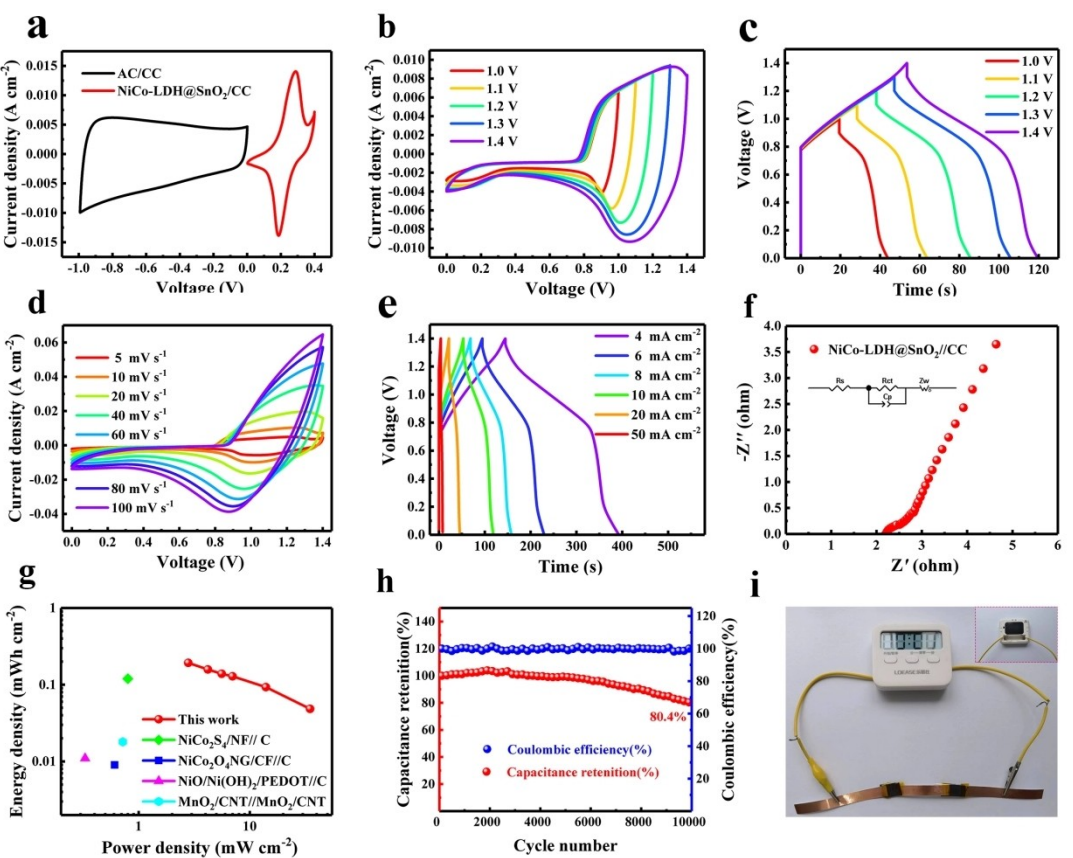


**Figure 5.** (a) CV curves of NiCo-LDH@SnO<sub>2</sub> and AC//CC at 50 mV s<sup>-1</sup>; (b) CV curves and (c) GCD curves of NiCo-LDH@SnO<sub>2</sub>//AC all-solid-state flexible ASC in different voltage ranges; (d) CV curves of the ASC at different scanning rates; (e) GCD curves of the ASC at different current densities; (f) EIS curve of the ASC; (g) Ragone plot of the ASC and comparison with other materials; (h) Cyclic stability test of the ASC for 5000 cycles at 20 mA cm<sup>-2</sup>; (i) Photographs of driven devices of one motor by the ASC in series.

spond to the oxidation peak and reduction peak of CV curve in Figure 4c respectively. Figure S1 shows the rate performance of NiCo-LDH@SnO<sub>2</sub>. It can be concluded by calculation that the capacitance at 2, 4, 6, 8, 10 and 20 mA cm<sup>-2</sup> are 1766, 1714.3, 1687.5, 1663.3, 1630 and 1415 mF cm<sup>-2</sup>, respectively. Compared with other active materials, NiCo-LDH@SnO<sub>2</sub> composites showed competitiveness (see Table S1). Figure 4e shows the EIS curve for NiCo-LDH@SnO<sub>2</sub>. (Figure S2 shows the equivalent circuit diagram). It can be seen that NiCo-LDH@SnO<sub>2</sub> composites exhibit lower charge transfer resistance (R<sub>ct</sub>) and equivalent series resistance (R<sub>s</sub>). They are 1.329 Ω and 0.328 Ω, respectively. In addition, the linear slope of NiCo-LDH@SnO<sub>2</sub> is higher in the low frequency range, indicating that the diffusion resistance of NiCo-LDH@SnO<sub>2</sub> is also lower than that of the NiCo-LDH sample.<sup>[44–45]</sup>

The mechanism of energy storage in electrochemical systems can be elucidated by pseudocapacitance analysis. Unlike traditional double layer capacitors, pseudocapacitors are caused by Faraday redox reactions on the surface of the active material. We can judge the energy storage mode of the electrode material by the b value, which can be calculated by the following formula.<sup>[45]</sup>

$$I = aV^b \quad (1)$$

I represents the peak current, V represents the scanning rate, and a is the parameter in different cases. According to this formula, we can calculate the value of b. When b=0.5 means the diffusion control process, when b=1 means the capacitive control process. After calculation, b<sub>1</sub> and b<sub>2</sub> are 0.88 and 0.86 respectively, which means that the capacitive control and the diffusion control process exist simultaneously in the practical application process. In addition, we can calculate the ratio of capacitive control to diffusion control by the following formula.<sup>[46]</sup>

$$I = K_1 V + K_2 V^{1/2} \quad (2)$$

I represents the total current, k<sub>1</sub>V and k<sub>2</sub>V<sup>1/2</sup> represent capacitive and diffusion processes, respectively. The capacitive contribution rate can be obtained by calculating the ratio of capacitance area to total area of CV curve. Figure 4g shows that the contribution rate of capacitive control of NiCo-LDH@SnO<sub>2</sub> is 79.4% at 8 mV<sup>-1</sup>. The contribution of capacitance control at other scan rates is shown in Figure S3. With the increase of scanning rate, the contribution rate of capacitance control corresponding to NiCo-LDH@SnO<sub>2</sub> electrode also gradually

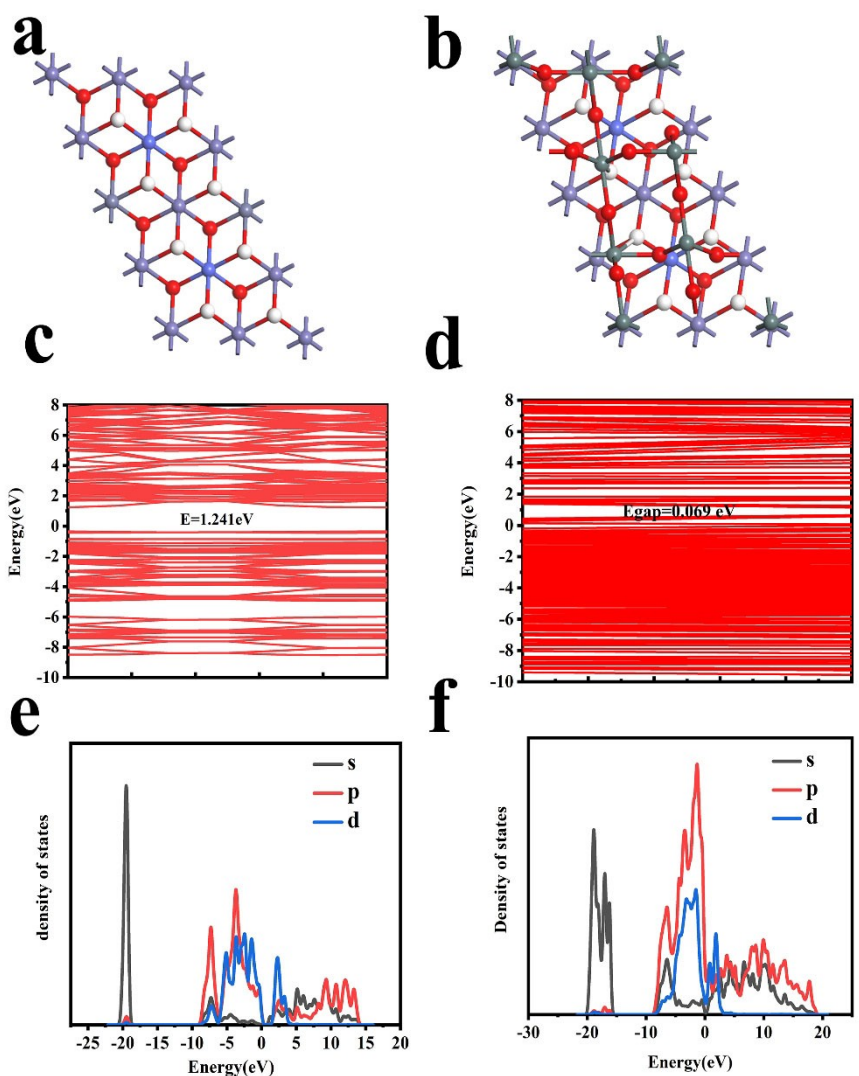


**Figure 6.** Theoretical roadmap of the achieved (a)NiCo–LDH and (b)NiCo–LDH@SnO<sub>2</sub> electrode materials. Electron band structure of (c) NiCo–LDH and (d)NiCo–LDH@SnO<sub>2</sub>. The DOS of (e) NiCo–LDH and (f) NiCo–LDH@SnO<sub>2</sub>.

increases in Figure 4h, which suggests that the capacitive process plays a dominant role in the overall capacity, and reveals the fast transfer kinetics of NiCo–LDH@SnO<sub>2</sub>. Figure 4i shows the results of 5000 cycles of the NiCo–LDH@SnO<sub>2</sub> at 20 mA cm<sup>-2</sup>. And the coulomb efficiency of NiCo–LDH@SnO<sub>2</sub> is basically maintained at 100%, showing that the Faraday redox reaction has good reversibility. The good cycle stability of NiCo–LDH@SnO<sub>2</sub> electrode material is demonstrated by the retention of 81.6% of the initial capacitance after 5000 cycles.

We have assembled an all-solid-state ASC with AC anode to further investigate the practical application value of NiCo–LDH@SnO<sub>2</sub> material. Figure 5a shows CV curves for the AC anode (-1–0.0 V) and NiCo–LDH@SnO<sub>2</sub> cathode (0–0.4 V) at a scan rate of 4 mV<sup>-1</sup>, demonstrating the feasibility of assembling 1.4 V all-solid-state ASC. And the Figure 5b shows the CV curve of the all-solid ASC under different voltage Windows. Even when the voltage window is extended to 1.4 V, the CV curve shape stays the same, showing that the ASC can operate stably under a wide voltage window. In Figure 5c, all

GCD curves are maintained well, indicating good electrochemical reversibility. Figure 5d shows the CV curve of the ASC at a scan rate of 5 to 100 mVs<sup>-1</sup>. The shape of the curve holds up well, showing that the ASC has good reversibility. The all-solid ASC calculated by the GCD curve in Figure 5e at 4, 6, 8, 10, 20 and 50 mA cm<sup>-2</sup> are 710, 580.7, 512, 475, 342.8 and 178.5 mF cm<sup>-2</sup>, respectively. And the rate performance of the ASC is shown in Figure S4.

The EIS curve of ASC is shown in Figure 5f. According to the fitting analysis, it can be concluded that the R<sub>s</sub> and R<sub>ct</sub> of ASC are 2.17 Ω and 0.615 Ω, and their low resistance values indicate the good ion transfer kinetics of all-solid-state ASC. Figure 5g shows the Ragone diagram of an all-solid-state ASC with a high energy density of 193 μWh cm<sup>-2</sup> at a power density of 2.8 mW cm<sup>-2</sup>. Even when the power density is 34.98 mW cm<sup>-2</sup>, the ASC can still have an energy density of 48.5 μWh cm<sup>-2</sup>. Comparing with other reported ASCs in Table S2, our ASC shows good energy storage performance. As can be seen from Figure 5h, the coulomb efficiency of all-solid ASC after 10,000

cycles at  $20 \text{ mA cm}^{-2}$  is about 100%, indicating that a highly reversible redox reaction occurs in the ASC. The cycle retention rate reached 80.4%, indicating that the ASC has excellent cycle stability during the long-term cycle. Two ASCs connected in series can successfully power the timer with a voltage of 2.8 V in Figure 5i, which shows the practical value of the ASC. The previous results show that NiCo–LDH@SnO<sub>2</sub> electrode materials have great application potential in the field of energy storage.

In order to deeply analyze the constructed NiCo–LDH@SnO<sub>2</sub> heterostructures, we utilized density-functional theory (DFT). The atomic models of NiCo–LDH and NiCo–LDH@SnO<sub>2</sub> were constructed separately and the structures were optimized (Figure 6a–b). Subsequently, we performed the energy bands (Figure 6c–d) and density of states (DOS) (Figure 6e–f) based on the optimized models. According to the results of simulations, it can be seen that the heterostructure has a significant increase in the Fermi energy level, which is consistent with our experimental results.

### 3. Conclusions

In summary, SnO<sub>2</sub> layer was prepared on CC surface by magnetron sputtering method, and then NiCo–LDH nanosheets were grown by hydrothermal reaction. Ni–Co LDH nanosheets interleaved with each other not only promoted the flow of the electrolyte, but also provided a large number of active sites, which made the Faraday redox reaction more adequate. At the same time, there is a synergistic effect between NiCo–LDH and SnO<sub>2</sub>, so the NiCo–LDH@SnO<sub>2</sub> composite not only exhibits a Cs of  $1766 \text{ mF cm}^{-2}$ , but also has a cyclic stability of 81.6%. Furthermore, an all-solid-state flexible ASC was fabricated using an AC anode. The device exhibits an energy density of  $193 \mu\text{Wh cm}^{-2}$  at a power density of  $2.8 \text{ mW cm}^{-2}$ . After 10,000 cycles, ASC showed a good cycle stability of 80.4%. Therefore, NiCo–LDH@SnO<sub>2</sub> provides a new scheme for the preparation of flexible supercapacitor materials.

### Supporting Information

Supporting Information is available from the author.

### Acknowledgements

This research were supported by grants from Science and Technology Research Project of Jilin Provincial Department of Education (JKH20220627KJ) and Natural Science Foundation of Jilin Province (202401011112JC).

### Conflict of Interests

The authors declare no conflict of interest.

### Data Availability Statement

The data that support the findings of this study are available from the corresponding author upon reasonable request.

**Keywords:** All-solid-state supercapacitors • Magnetron sputtering • SnO<sub>2</sub> • NiCo–LDH • High-performance

- [1] L. Duan, L. Zhao, H. Cong, X. Zhang, W. Lu, C. Xue, *Small* **2019**, *15* (7), e1804347.
- [2] X. Hou, Q. Zhang, L. Wang, G. Gao, W. Lu, *ACS Appl. Mater. Interfaces* **2021**, *13* (10), 12432–12441.
- [3] J. A. Isaac, D. Devaux, R. Bouchet, *Nat. Mater.* **2022**, *21* (12), 1412–1418.
- [4] A. Amiri, A. Bruno, A. A. Polycarpou, *Carbon Energy* **2023**, *5* (5).
- [5] R. M. Bhattacharai, K. Chhetri, N. Le, D. Acharya, S. Saud, M. C. H. P. L. Nguyen, S. J. Kim, Y. S. Mok, *Carbon Energy* **2023**, *6*.
- [6] M. Peng, L. Wang, L. Li, X. Tang, B. Huang, T. Hu, K. Yuan, Y. Chen, *Adv. Funct. Mater.* **2021**, *32*.
- [7] Y. Li, B. Cheng, F. Jiao, K. Wu, *ACS Appl. Mater. Interfaces* **2020**, *12* (14), 16298–16307.
- [8] T. Liu, Y. Qu, J. Liu, L. Zhang, B. Cheng, J. Yu, *Small* **2021**, *17* (49), e2103673.
- [9] A. R. Selvaraj, I. S. Raja, D. Chinnadurai, R. Rajendiran, I. Cho, D. W. Han, K. Prabakar, *J. Energy Storage* **2022**, *46*.
- [10] T. A. Wani, G. Suresh, *J. Energy Storage* **2021**, *44*.
- [11] L. Wang, M. Peng, J. Chen, T. Hu, K. Yuan, Y. Chen, *Adv. Mater.* **2022**, *34*, e2203744.
- [12] X. Guan, M. Huang, L. Yang, G. Wang, X. Guan, *Chem. Eng. J.* **2019**, *372*, 151–162.
- [13] J. Cui, J. Yang, J. Man, S. Li, J. Yin, L. Ma, W. He, J. Sun, J. Hu, *Electrochim. Acta* **2019**, *300*, 470–481.
- [14] X. Liang, H. He, X. Yang, W. Lü, L. Wang, X. Li, *J. Energy Storage* **2021**, *42*.
- [15] L. Wang, M. Peng, J. Chen, X. Tang, L. Li, T. Hu, K. Yuan, Y. Chen, *ACS Nano* **2022**, *16*, 2877–2888.
- [16] Z.-A. Hu, Y.-L. Xie, Y.-X. Wang, L.-P. Mo, Y.-Y. Yang, Z.-Y. Zhang, *Mater. Chem. Phys.* **2009**, *114* (2–3), 990–995.
- [17] Y. Liu, Y. Jiao, Z. Zhang, F. Qu, A. Umar, X. Wu, *ACS Appl. Mater. Interfaces* **2014**, *6* (3), 2174–84.
- [18] S. N. Pasawale, P. R. Deshmukh, C. D. Lokhande, *Appl. Surf. Sci.* **2011**, *257* (22), 9498–9502.
- [19] H. Li, S. Lin, H. Li, Z. Wu, Q. Chen, L. Zhu, C. Li, X. Zhu, Y. Sun, *Small Methods* **2022**, *6*, e2101320.
- [20] H. Liang, J. Lin, H. Jia, S. Chen, J. Qi, J. Cao, T. Lin, W. Fei, J. Feng, *J. Power Sources* **2018**, *378*, 248–254.
- [21] S. Ramandi, M. H. Entezari, *J. Energy Storage* **2022**, *56*.
- [22] C. Zhang, L. Zhang, Q. Liu, Y. Ding, L. Cheng, M. Wu, Z. Li, *Appl. Surf. Sci.* **2022**, *602*.
- [23] T. Zhao, C. Liu, T. Meng, W. Deng, L. Zheng, F. Yi, A. Gao, D. Shu, *Small* **2022**, *18* (20), e2201286.
- [24] F. Zhu, W. Liu, Y. Liu, W. Shi, *Chem. Eng. J.* **2020**, *383*.
- [25] M. Liu, L. Wang, X. Yu, H. Zhang, H. Zhang, S. Li, F. Huang, *Energy* **2022**, *238*.
- [26] J. Zou, D. Xie, J. Xu, X. Song, X. Zeng, H. Wang, F. Zhao, *Appl. Surf. Sci.* **2022**, *571*.
- [27] S. Asaithambi, P. Sakthivel, M. Karuppaiah, G. U. Sankar, K. Balamurugan, R. Yuvakkumar, M. Thambidurai, G. Ravi, *J. Energy Storage* **2020**, *31*.
- [28] S. Asaithambi, P. Sakthivel, M. Karuppaiah, R. Yuvakkumar, K. Balamurugan, T. Ahamad, M. A. M. Khan, G. Ramalingam, M. K. A. Mohammed, G. Ravi, *J. Energy Storage* **2021**, *36*: 102402.
- [29] D. Bejjanki, G. Uday Bhaskar Babu, K. Kumar, S. Kumar Puttapati, *Mater. Today: Proc.* **2023**, *78*, 74–79.
- [30] E. Samuel, T.-G. Kim, C.-W. Park, B. Joshi, M. T. Swihart, S. S. Yoon, *ACS Sustainable Chem. Eng.* **2019**, *7*, 14031–14040.
- [31] V. Shanmugapriya, S. Arunpandian, G. Hariharan, S. Bharathi, B. Selvakumar, A. Arivarasan, *J. Alloys Compd.* **2023**, *935*.
- [32] S. Vargheese, R. S. Kumar, R. T. R. Kumar, J.-J. Shim, Y. Haldorai, *J. Energy Storage* **2023**, *68*: 107671.
- [33] R. Adalati, A. Kumar, G. Malik, R. Chandra, *Dae Solid State Physics Symposium* **2019**, 2020.
- [34] M. I. Ionescu, X. Sun, B. Luan, *Can. J. Chem.* **2015**, *93*, 160–164.
- [35] H. Shen, B. Wei, D. Zhang, Z. Qi, Z. Wang, *Mater. Lett.* **2018**, *229*, 17–20.

- [36] B. Wei, H. Liang, D. Zhang, Z. Qi, H. Shen, Z. Wang, *Materials for Renewable and Sustainable Energy* **2018**, 7 (2).
- [37] B. Wei, H. Liang, D. Zhang, Z. Wu, Z. Qi, Z. Wang, *J. Mater. Chem. A* **2017**, 5 (6), 2844–2851.
- [38] X. Xu, S. Chang, Z. Hong, Y. Zeng, H. Zhang, P. Li, S. Zheng, Z. Wang, S. Duo, *Nanotechnology* **2021**, 33 (5).
- [39] Y. Jiang, B. Cai, Y. Yang, F. Yu, Y. Sun, X. Qi, L. Wang, X. Li, X. Yang, *J. Energy Storage* **2022**, 56.
- [40] V. Molahalli, V. S. Bhat, A. Shetty, D. Hundekal, A. Toghan, G. Hegde, *J. Energy Storage* **2023**, 69.
- [41] H. Du, F. Ding, J. Zhao, X. Zhang, Y. Li, Y. Zhang, J. Li, X. Yang, K. Li, Y. Yang, *Appl. Surf. Sci.* **2020**, 508.
- [42] S. Li, Y. Luo, C. Wang, M. Wu, Y. Xue, J. Yang, L. Li, *J. Alloys Compd.* **2022**, 920.
- [43] Y. Zhu, H. Xu, P. Chen, Y. Bao, X. Jiang, Y. Chen, *Electrochim. Acta* **2022**, 413.
- [44] G. Xiang, Y. Meng, G. Qu, J. Yin, B. Teng, Q. Wei, X. Xu, *Sci. Bull.* **2020**, 65, 443–451.
- [45] S. Zhao, C. Li, X. Zhang, N. Li, T. Wang, X. Li, C. Wang, G. Qu, X. Xu, *Sci. Bull.* **2023**, 68, 56–64.
- [46] Q. Hu, C. Kang, S. Cao, C. Zhou, Q. Liu, *J. Alloys Compd.* **2021**, 883.
- [47] S. Tian, X. Zhang, Z. Zhang, *Chem. Eng. J.* **2021**, 409.

---

Manuscript received: February 26, 2024

Revised manuscript received: March 29, 2024

Accepted manuscript online: April 7, 2024

Version of record online: May 7, 2024

---